

Journal of Materials Chemistry A

Accepted Manuscript



This is an *Accepted Manuscript*, which has been through the Royal Society of Chemistry peer review process and has been accepted for publication.

Accepted Manuscripts are published online shortly after acceptance, before technical editing, formatting and proof reading. Using this free service, authors can make their results available to the community, in citable form, before we publish the edited article. We will replace this *Accepted Manuscript* with the edited and formatted *Advance Article* as soon as it is available.

You can find more information about *Accepted Manuscripts* in the [Information for Authors](#).

Please note that technical editing may introduce minor changes to the text and/or graphics, which may alter content. The journal's standard [Terms & Conditions](#) and the [Ethical guidelines](#) still apply. In no event shall the Royal Society of Chemistry be held responsible for any errors or omissions in this *Accepted Manuscript* or any consequences arising from the use of any information it contains.

Improvement of the photocatalytic degradation property of ZnO atomic layer deposition thin films: Interplay between film properties and functional performances

Cite this: DOI: 10.1039/x0xx00000x

Received 00th January 2012,
Accepted 00th January 2012

DOI: 10.1039/x0xx00000x

www.rsc.org/

V.Rogé,^{ab} N. Bahlawane,^a G.Lamblin^a, I.Fechete^b, F.Garin^b, A.Dinia^c and D.Lenoble^{a*}

We evidence in this work the impact of the stoichiometry in ZnO nanofilms grown by Atomic Layer Deposition (ALD) on their photocatalytic properties. We point out the capital importance of the hydrogen incorporation and propose here a model explaining the presence of Zn-OH impurities in the form of a ZnO_xH_y amorphous matrix hosting ZnO crystallites. We evidence that this phase prevails in films grown at low temperatures and prevents the photoluminescence and photocatalytic activity of the ZnO films. We also point out that high temperature ALD processes promote the preferential growth of the ZnO films in the (002) orientation, leading to a significant increase of the films wettability and so their photocatalytic degradation performances.

Introduction

The use of photocatalytic materials for water remediation is an innovative rapidly growing field. Several semiconductors were investigated as a mean to use the abundant solar energy to clear water¹. Among them, ZnO is a well-known and interesting photocatalyst due to its intrinsic properties like its direct band gap around 3.2 eV and its excitons binding energy around 60 meV. Thus, ZnO absorbs light in the UV range and exhibits luminescent properties even at room temperature². Furthermore, ZnO is readily available, biocompatible, thermally stable and can be synthesized in many different nanostructures³. As a consequence, ZnO is a potential material for optical and electronic devices like UV laser diodes, photo detectors, piezoelectric nano-generators, solar cells and photocatalysis⁴. The photocatalytic performance of ZnO has been widely studied for various nanostructures like nano-films⁵, nano-wires⁶, nano-particles⁷ or nano-platelets^{8,9}. Those studies have pointed out the chemical degradation of different dyes like methylene blue¹⁰, rohdamine b¹¹, methyl orange¹², or other organics like salicylic acid¹³, chlorophenol and chlorobenzene¹⁴ when ZnO nanostructures are illuminated under UV radiation. ZnO can be synthesized using many different processes with a significant impact of the resulting properties. The synthesis processes can be regarded as liquid-based or dry processes. The

liquid phase synthesis relies on hydrothermal, precipitation and sol-gel processes. These methods allow the synthesis of diverse nanostructures of ZnO at low temperature^{15,16}. The low temperature is however associated with potential presence of impurities including carbon^{17,18}. The dry synthesis processes are either chemical (Chemical Vapour Deposition: CVD) or physical (Physical Vapour Deposition). The PVD processes rely on thermal evaporation or the sputtering of a source material under high vacuum¹⁹. The PVD processes yield in general high quality coatings, but they are inherently line-of-sight which is not compatible with the deposition on powders. The activation of the deposition reactions in CVD can be thermal or assisted by plasma or a laser beam; and the surface might be simultaneously or sequentially (Atomic layer Deposition) exposed to the deposition reactants. This latter mode (ALD) enables the growth of conformal films. High temperature CVD processes have the advantage of growing structures with high crystallinity and low defect concentrations²⁰.

Due to the difference in the growth mechanism, precursors used or growth temperature for all synthesis processes, particular defects can be created in the ZnO structure. CVD usually leads to high quality films due to the high temperature used during the process, nevertheless defects like zinc vacancies/interstitial or oxygen vacancies/interstitial might be present²¹. Adjusting the partial pressure of oxygen relative to Zn precursor is an

efficient way to optimize the films stoichiometry²². When it comes to the growth of thin films on 3D templates, relevant to photocatalytic applications, like porous substrates with high aspect ratios, the ALD has an excellent advantage. The perfect conformality of coatings made by ALD opens new possibilities for the design of innovative photocatalysts. Systems like core/shell heterostructures composed of a nanoparticles of SnO₂ or TiO₂, covered homogeneously by a ZnO film as a shell can then be accessible^{23,24}. These heterostructures are particularly interesting for water photocatalytic cleaning applications. The sequential exposure of the surface to the deposition reactants in the ALD enables the use of highly reactive precursors which considerably lowers the temperature of the process. The development of low temperature ZnO by ALD has already been reported in the literature²⁵. The ALD of ZnO can be performed starting from room-temperature, but no report addresses the impact of the growth temperature on the photocatalytic performance of the films. In this work, we thoroughly study the impact of the growth temperature of ZnO by ALD on the photocatalytic degradation performances. These performances are explained by deeply investigating the resulting physico-chemical properties of the ZnO films in order to report, for the first time to our knowledge, specific properties of low temperature ZnO driving the photocatalytic performances. Our work clearly establishes the interplay between the nanofilms stoichiometry, morphology, crystalline properties and their photocatalytic performances.

Experimental

Materials and methods

High purity grade single side polished (100) silicon wafers were used as substrates. Concerning the ZnO ALD deposition, Diethyl Zinc (DEZ 99.99 % from Sigma-Aldrich) was used as a zinc source and deionized water as an oxidant. The reaction took place in a commercial gas phase ALD TF200 from Beneq Company. The reactants were kept in canisters under vacuum at 18 °C and their vapours were injected into the reaction chamber without any carrier gas. The reaction was realized at low pressure (5 mBar) using dry nitrogen as a purge gas. During the ALD cycle, the surface was exposed for 200 ms to DEZ vapour and then for another 200 ms to the vapour of water. The purge between these steps was performed for 2 s under a nitrogen flow of 350 sccm. These conditions enable reaching the surface saturation in each step, and the purge is long enough to suppress the occurrence of parasitic CVD reactions. The number of cycles has been arbitrary fixed at 500 cycles, to grow layers around 100 nm of ZnO irrespective of the growth temperature. The thickness was evaluated from cross-section SEM pictures shown in the Figure 1.

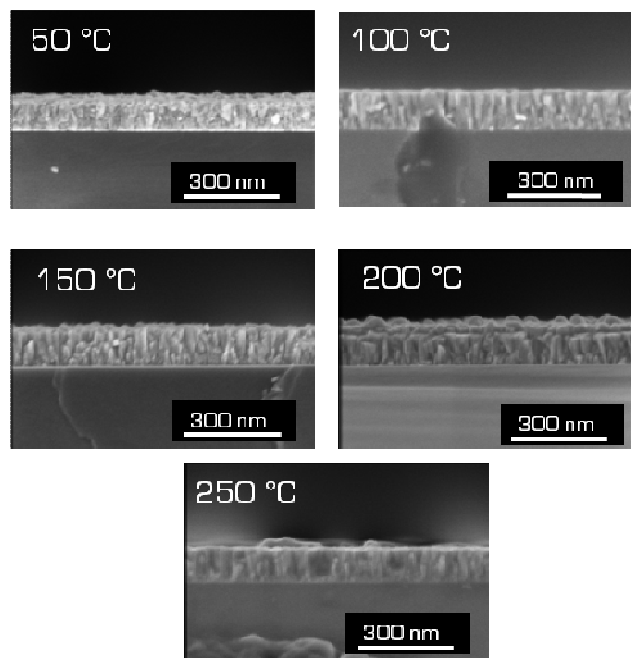


Figure 1: SEM cross section images of ZnO ALD thin films grown at different temperatures. The thickness has been evaluated around 100 nm.

A Residual Gas Analyser (RGA) Microvision 2 from MKS was used to characterize exhaust gas from the ALD system as a function of the temperature. Scanning Electron Microscopy (SEM) was implemented to assess the morphology of the layers, using a high resolution Helios Nanolab 650 microscope from FEI Company. The working acceleration voltage was set at 2 kV for a current of 25 mA. Atomic Force Microscopy (AFM) was performed with an Innova AFM from Bruker, operated in tapping mode. The specific surface area of the ZnO nanofilms has been calculated from the topography extracted from 1 cm² AFM images by using the software Gwyddion, and used for the normalisation of the degradation rate. The optical properties of the ZnO films, as well as monitoring of the photocatalytic tests were investigated with a UV-visible spectrometer Infinite M1000 pro from TECAN. Photoluminescence experiments for the different ZnO nanofilms were performed under a 280 nm excitation wavelength while detecting from 300 to 700 nm. The methylene blue absorbance was measured from 500 to 700 nm. The chemical composition of the films was obtained by X-ray photoelectron spectroscopy (XPS) with an Axis Ultra DLD X-ray spectrometer from Kratos Analytical Company, working with a monochromatic Al K α 1 x-ray source at 150 W. A deconvolution of the high resolution O_{1s} peak is used to quantify the relative abundance of Zn-OH and Zn-O bondings in the deposited films. The crystallographic structure of the films have been analysed by X-ray diffraction (XRD), using a D8 discover diffractometer from Bruker with a Cu K α X-ray source ($\lambda=0,1542$ nm). Water contact angle was measured using a Krüss DSA16 Easy Drop USB contact angle meter.

Photocatalytic experiments

The photocatalytic experiments were performed in a 6 wells plate, in 5 ml of a 5 mg.l⁻¹ solution of methylene blue (MB), under constant agitation. The samples to characterize were placed in individual wells. They were cut in 2 cm² pieces in order to have a comparable exposed active surface. The methylene blue acts here as a probe molecule to evaluate the photodegradation performance. The evolution of the MB concentration was followed by optical absorption measuring the absorbance at 666 nm with a UV-visible spectrometer. The light source used for the photocatalytic degradation was a 365 nm UV lamp, delivering a measured power of 2.28 mW.cm⁻² at the surface of the ZnO films.

Determination of ALD window temperature

The ALD temperature window of ZnO has been determined after a study of the diethyl zinc stability versus the temperature. DEZ has been injected into the reactor chamber under different temperatures, and the by-products of its thermolysis were analysed by RGA. The dominant initial decomposition step of DEZ is known to be the Zn-C bond homolysis²⁶, leading to C₂H₆, C₂H₄, and H₂. The intensities of C₂H₄ and H₂ were monitored as a function of the temperature and the obtained results are shown in figure 2. Both molecules were not detected below 250 °C which means that DEZ is thermally stable. Above 250 °C, the signal intensity relative to C₂H₄ and H₂ increases with the temperature, indicating the occurrence of the thermolysis reaction. This result indicates that the maximum temperature applicable for the ALD regime is 250 °C. It is worth mentioning that the hydrolysis of DEZ can occur already below room temperature²⁷. Therefore we focused our work on the ALD of ZnO from 50 °C up to 250 °C, in order to characterize their photocatalytic performances. It is worth mentioning that purging water from the reactor below 50°C is highly demanding.

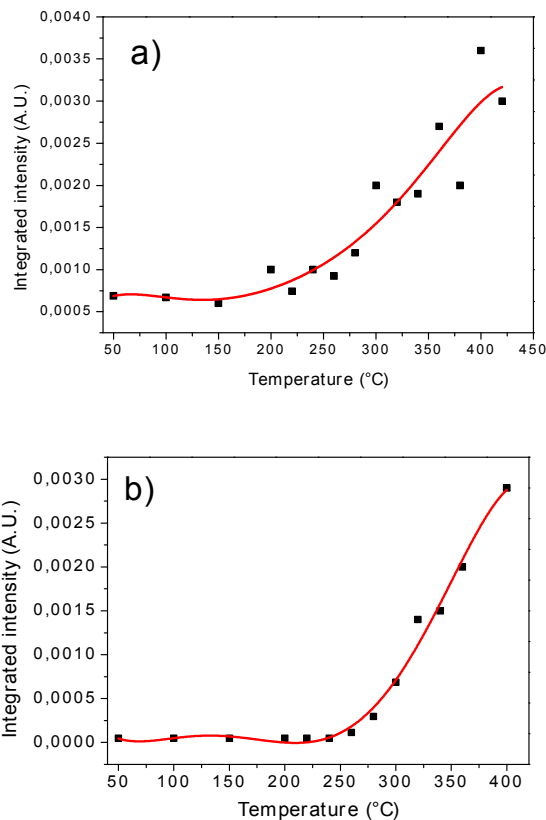
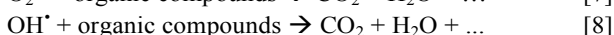
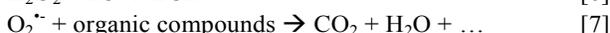
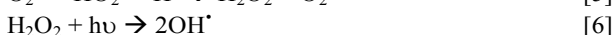
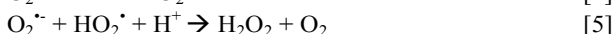
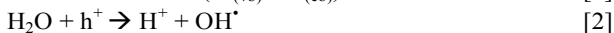
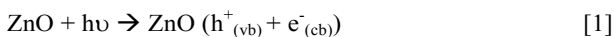


Figure 2: RGA analysis of a) ethylene and b) hydrogen in the exhaust gas as a function of the reactor temperature (50 °C to 400 °C) using an inlet gas of N₂-DEZ.

Results and Discussion

Photocatalytic performance:

When ZnO is irradiated with a light whose energy is above the band gap, an electron (e⁻)/hole (h⁺) pair can be created. The highly reactive carriers (e⁻ and h⁺) will produce hydroxyl (OH[•]) and superoxide radicals (O₂^{•-}) when reacting with water or oxygen at the ZnO surface (Figure 3). OH[•] is a strong oxidizing radical that can react with C-C bonds in organic molecules. O₂^{•-} is a reducing specie that is able to reduce H₂O into H₂O₂. H₂O₂ under UV light decomposes in OH[•]. The well admitted mechanism for a photocatalytic degradation can be described as follow^{28,29,30}:



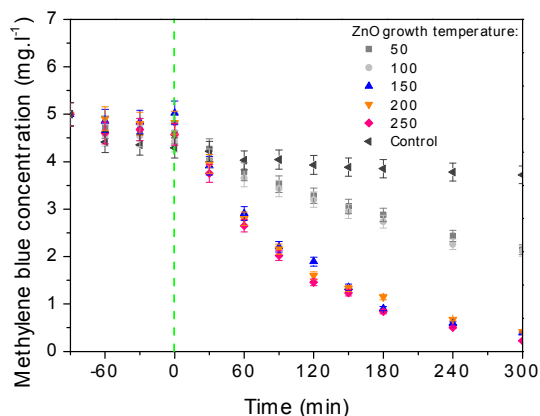
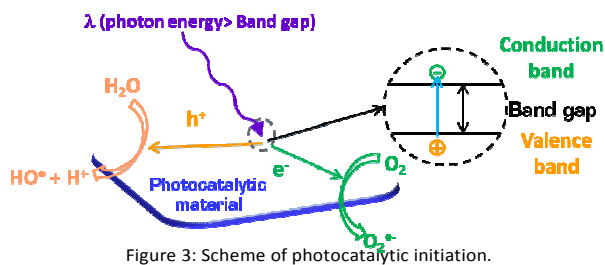


Figure 4: Photocatalytic degradation of methylene blue under UV light (365 nm – 8 W) over ZnO films grown at different temperatures. Lightning corresponds to time=0.

The investigation of the photocatalytic activity of the ZnO films with similar thicknesses shows a clear correlation between the growth temperature and the degradation kinetic of methylene blue (Figure 4). Before switching on the UV light, ZnO surfaces have been exposed to the methylene blue solution during 90 minutes. This protocol induces a slight decrease of the methylene blue concentration in the liquid solution. This is attributed to the methylene adsorption at the sample surfaces. After switching on the UV light, one can notice a continuous decrease of the methylene blue concentration matching a

pseudo first order kinetic law: $\ln(C_0/C) = kt$. The degradation rate k (min^{-1}) of all ZnO nanofilms has been extracted when plotting $\ln(C_0/C)$ versus the irradiation time (Figure 5). The ZnO films grown at 50 °C and 100 °C exhibit a degradation rate constant (normalised to the surface area) in the range of $5.10^{-4} \text{ min}^{-1} \cdot \text{cm}^{-2}$ (Table 1). More than a two fold improvement is observed for the films grown above 150 °C, and the degradation rate ranges from $1.75.10^{-3}$ to $2.15.10^{-3} \text{ min}^{-1} \cdot \text{cm}^{-2}$. Our photocatalytic degradation rate constant (around $2.15.10^{-3} \text{ min}^{-1} \cdot \text{cm}^{-2}$) is similar to the degradation rate constant (normalised to the exposed surface) reported for nanofilms obtained by electrodeposition, i.e. $3.1.10^{-3} \text{ min}^{-1} \cdot \text{cm}^{-2}$, while being at least 3 orders of magnitude higher than isolated nanostructures like nanoparticles, tetrapods or nanowires grown by wet or dry chemistries (Table 2). Table 2 also reports a very low degradation rate of nanofilms grown by ALD (Y.Cao *et al.*); this further highlights the excellent photocatalytic performance of our films. Therefore, a detailed investigation of the properties of our nanofilms is required to better identify the rationales controlling the photocatalytic responses of our ZnO nanofilms.

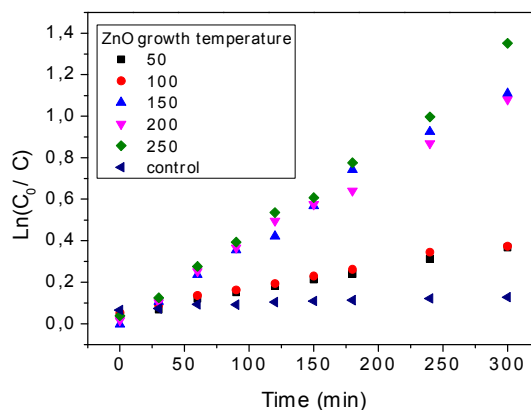


Figure 5: Plot of $\ln(C_0/C)$ versus time for ZnO ALD grown at different temperatures in order to determine the first order degradation rate constant.

Table 1: First order rate constant normalised to the surface exposed of the ZnO nanofilms grown at different temperatures, calculated from the linear plot of $\ln(C_0/C)$ versus the irradiation time.

ZnO growth temperature (°C)	First order rate constant normalised to the surface exposed ($\text{min}^{-1} \cdot \text{cm}^{-2}$)
50	5.10^{-4}
100	6.10^{-4}
150	$17.5.10^{-4}$
200	$19.5.10^{-4}$
250	$21.5.10^{-4}$
Silicon substrate (control)	2.10^{-4}

Table 2: Bibliographic study of the first order degradation rate constant for different ZnO structures grown by different techniques.

ZnO structures	Synthesis technic	Degradation constant k (min ⁻¹)	Exposed surface (cm ²)	Degradation rate constant normalized to the surface (min ⁻¹ .cm ⁻²)	References
Nanofilm	Electrodeposition	0,0062	2	3.10.10 ⁻⁰³	31
Nanofilm	ALD	0,0006	79	7.59.10 ⁻⁰⁶	32
Nanoparticles	Wet synthesis	0,008	15360	5.21.10 ⁻⁰⁷	33
Nanoparticles	Sol-Gel	0,016	47300	3.38.10 ⁻⁰⁷	34
Nanoparticles	Hydrothermal	0,05	22950	2.18.10 ⁻⁰⁶	35
Tetrapods	Vapour phase	0,34	1100	3.09.10 ⁻⁰⁴	35
Nanowires	Vapour phase	0,015	20050	7.48.10 ⁻⁰⁷	36

Physical and chemical properties of ZnO thin films:

The morphology of the obtained ZnO films was investigated by SEM as shown figure 6. The micrographs reveal conformal ZnO films covering the entire surface of the sample and composed of compact grains. The surface morphology shows symmetrical grains below 150 °C, while grains with enhanced elongation are observed above this temperature. This evolution of the topography has been monitored by AFM to determine the surface roughness. At low temperature, the roughness of the film is around Ra=11 nm, whereas a roughness of Ra=20 nm was measured for films grown at 250 °C. This change in the surface roughness is incremental, which explains a non-significant change in the specific surface area estimated from AFM pictures (not shown).

The differences in the morphology and specific surface between ZnO films grown at different temperatures are not significant enough to justify such variation of their photocatalytic activity. A study of the physico-chemical properties of the ZnO is therefore needed to better allocate the origin of this phenomenon.

The photoluminescence for ZnO films obtained at various growth temperatures is depicted in figure 7a. ZnO usually exhibits two luminescent bands. The narrow one in the near visible region, around 380 nm (3.2 eV), corresponds to the radiative exciton recombination in the material. It can also be reported as the near band edge emission (NBE). This peak is attributed to the direct electronic band gap of the crystal³⁷. An intense and narrow peak is characteristic for a highly crystalline ZnO structure^{38,39,40}. A second peak can be found in the visible region of the spectrum. The origin of this broad peak, with a maximum often in the green region around 580 nm (2.33 eV), is still debated in the literature^{41,42}, but it is commonly attributed to deep level defects (DLE) in the material like zinc vacancies, zinc interstitial, oxygen vacancies and oxygen anti-sites⁴³.

As depicted in figure 7a, low temperature processes lead to films with a broad and intense luminescent band from 500 to 700 nm without any resolved excitonic peak. With increasing

deposition temperature, the broad band intensity vanishes while the NBE peak intensifies. It is worth mentioning that the narrow peak observed at 560 nm on the spectrum corresponds to the double wavelength of the excitation source, and has no relation with our samples. This change in the optical properties of ZnO can be assigned either to chemical or structural differences. Zhou et al. have shown that the presence of Zn(OH)₂ at the surface of ZnO quantum dots quenches the ZnO NBE signal⁴⁴. Same authors have also shown that the thermal decomposition of Zn(OH)₂ leads to ZnO quantum dots that exhibit a clear NBE luminescence. Absorption measurements are displayed in Tauc plots (Figure 7b) to determine the optical bandgap of our nanofilms. The optical absorption is similar for ZnO nanofilms grown above 50 °C, this leads to an optical bandgap of 3.3 eV, very close to the values reported for pure ZnO crystals⁴⁵, and matching the wavelength of the excitonic peak (3.2 eV) observed in photoluminescence. For the ZnO grown at 50 °C, the optical bandgap is significantly higher, around 3.5 eV, highlighting the variation of the “ZnO” nanofilms properties. This corroborates with the photoluminescence spectrum showing a significant increase of the photoluminescence response in the range of the visible wavelength and the lack of photoluminescence originated from the radiative recombination of excitons close to the optical band gap. The formation of –OH bonds is inherent to the ALD process used in this study⁴⁶. It is thus very plausible to retrieve a fraction of these OH bonds within the bulk of the films, especially those grown at low temperatures (because of uncompleted reaction between –OH and DEZ with the used exposure time). A high concentration of hydrogen impurity might even yield an amorphous hydrogenated ZnO_xH_y phase. This hypothesis would be in line with the observed intense broad luminescence peak in the visible spectral range for films grown at low temperatures, and the emergence of the NBE luminescent signal for films grown above 150 °C.

XPS measurements have been carried out to verify this hypothesis (Table 3). Analyses have been performed after an etching of the surface (around 10 nm) with an argon ion beam in order to probe the bulk of the ZnO films. XPS analyses confirm the presence of Zn-OH bonding in the bulk of the

grown film at low temperatures⁴⁷. As seen in figure 8a, the high resolution O1s peak can be deconvoluted in two components: Zn-O bonding at 530.7 eV \pm 0.2 eV and Zn-OH bonding at 532.2 eV \pm 0.2 eV. The relative fraction of Zn-OH bonding is around 30 % for films grown at 50 °C. This fraction is two

folds lower for films grown at 100 °C with a fraction of 15%, and decreases still below 10 % for films grown at 250 °C (figure 8b). The exact positions of the peaks, as well as the relative binding energies are depicted in Table 3.

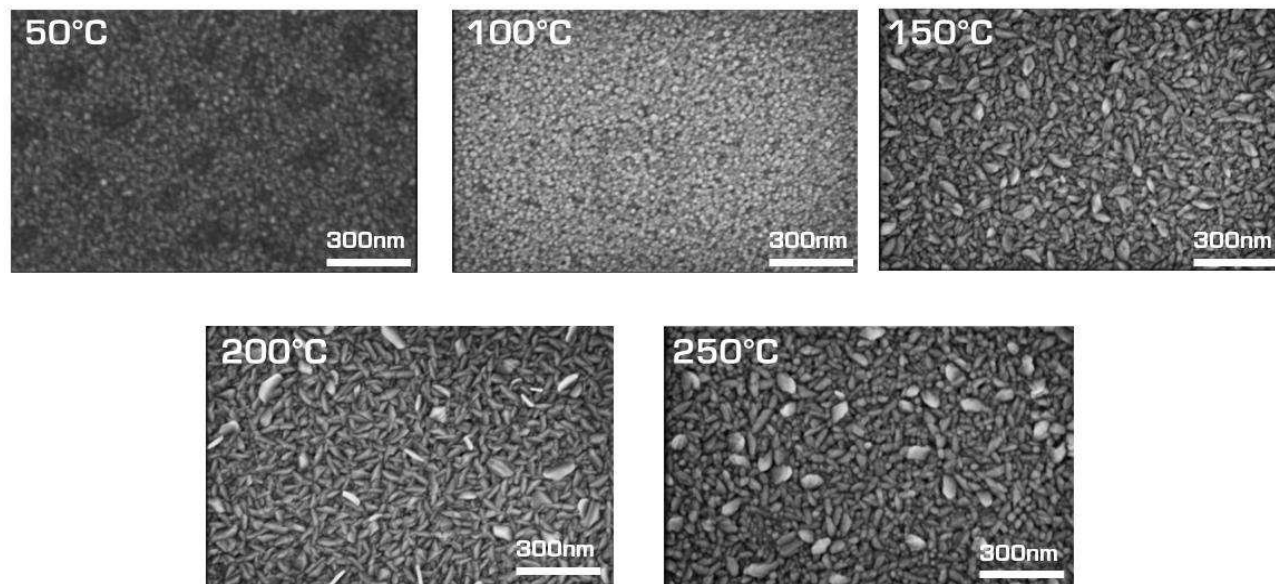


Figure 6: Surface morphology of ZnO films by SEM pictures as a function of the growth temperature.

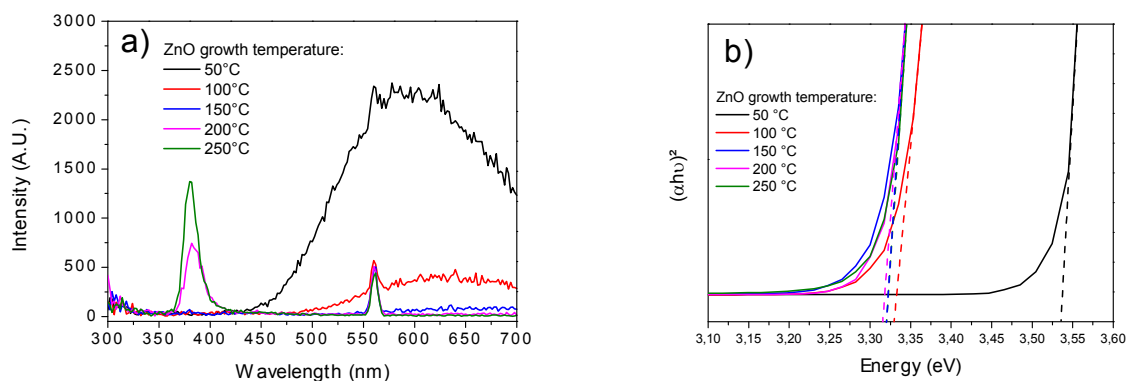


Figure 7: Photoluminescence spectrum (a) and Tauc plots (b) of ZnO films grown at different temperatures (50 °C, 100 °C, 150 °C, 200 °C, 250 °C).

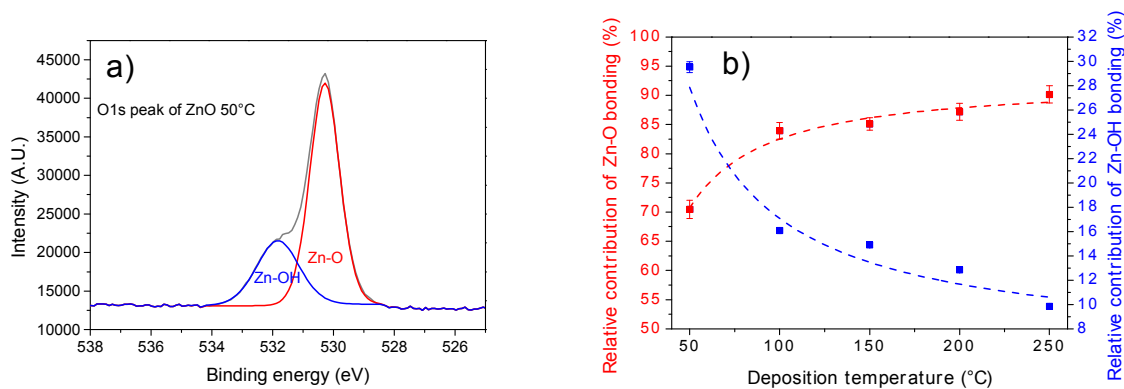


Figure 8: a) XPS O1s high resolution spectrum of the ZnO film grown at 50 °C, the two deconvolutions appear in blue for the Zn-OH bonding and in red for the Zn-O. b) Evolution of the relative concentration of Zn-OH bonding (in blue) and the Zn-O bonding (in red).

Table 3: XPS results presenting the position and the relative contribution of the Zn-OH and Zn-O bonding for films grown at different temperatures.

Sample		Peak position BE ($\pm 0,1\text{eV}$)	Zn LMM ($\pm 0,1\text{eV}$)	Modified Auger parameter α' (eV)		Peak position BE ($\pm 0,1\text{eV}$)	FWHM ($\pm 0,2\text{eV}$)	Relation contribution (%)	
ZnO 50 °C	Zn2p	1021,9	987,8	2009,8		O1s (Zn-O)	530,7	1,2	70
						O1s (Zn-OH)	532,3	1,6	30
ZnO 100 °C	Zn2p	1022,0	988,2	2010,3		O1s (Zn-O)	530,7	1,2	84
						O1s (Zn-OH)	532,2	1,7	16
ZnO 150 °C	Zn2p	1021,8	988,7	2010,5		O1s (Zn-O)	530,6	1,5	85
						O1s (Zn-OH)	532,2	1,8	15
ZnO 200 °C	Zn2p	1021,8	988,7	2010,5		O1s (Zn-O)	530,5	1,2	87
						O1s (Zn-OH)	532,1	1,6	13
ZnO 250 °C	Zn2p	1021,8	988,7	2010,5		O1s (Zn-O)	530,7	1,2	90
						O1s (Zn-OH)	532,4	1,5	10

The modified Auger parameter (α') has been estimated by adding the binding energy of the Zn2p_{3/2} peak and the kinetic energy of the LMM Auger peak (Table 3). Figure 9 shows the modified Auger parameter as a function of the growth temperature. In the case of ZnO synthesised above 150 °C, α' is perfectly matching the theoretical α' of bulk ZnO⁴⁸. However, for the ZnO nanofilms grown under 150 °C, α' is significantly lower and evidences different chemical states of Zn in these nanofilms.

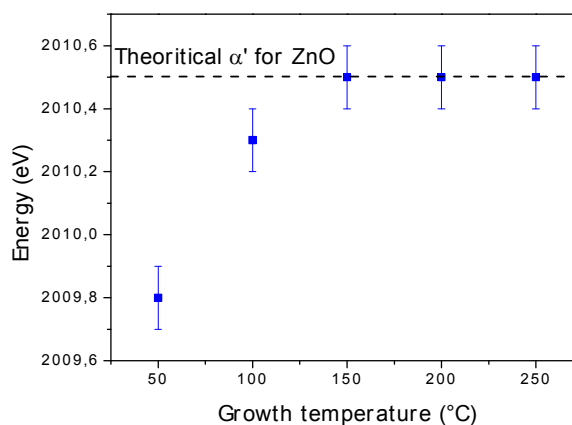


Figure 9: Modified Auger parameter calculated for ZnO ALD thin films grown at different temperatures. The linear dot line corresponds to the theoretical modified Auger parameter for bulk ZnO.

XPS studies indubitably reveal that ZnO nanofilms grown at low temperature are contaminated with hydrogen impurity.

Interstitial hydrogen and/or a segregated ZnO_xH_y phase are plausible. Since interstitial hydrogen is expected to induce a perceptible variation of the lattice parameters⁴⁹. XRD measurements have been carried out to clarify this issue. According to the X-ray diffractograms reported in figure 10, all ZnO nanofilms exhibit a hexagonal wurtzite structure with identical lattice parameters. An improved crystallinity is noticed when the growth temperature is increased. Lattice parameters have been calculated in the case of the hexagonal wurtzite structure by applying the following formula:

$$d_{hkl} = \frac{1}{\sqrt{\frac{4}{3a^2}(h^2 + k^2 + hk) + \frac{l^2}{c^2}}} \quad [9]$$

Where d_{hkl} is the distance between two lattice planes. h, k, l are the Miller indices and a, b, c the lattice parameters of the hexagonal wurtzite structure. From the (100) and the (110) diffraction peaks, the a and b parameters have been determined ($a=b$). From the (002) diffraction peak, we have estimated the c parameter. The values obtained are in very good agreement with the published lattice parameters⁵⁰ and are comparable regardless of the growth temperature (Table 4). No lattice distortion is evidenced, making the presence of interstitial hydrogen very unlikely. Segregated ZnO_xH_y phase is more probable together with the noticed change of the preferential crystalline orientation of the nanofilms according to the growth temperatures. There is a range of temperature between 100 °C and 150 °C where the (100) peak is dominant, whereas at higher temperatures its contribution lowers, and the (002) orientation becomes predominant. This crystalline texturation of the films is emphasized in figure 11 when plotting the calculated ratio of the XRD peak intensities (002)/(101). This ratio is five times more important for the films grown at 250 °C versus the ones obtained at 50 °C.

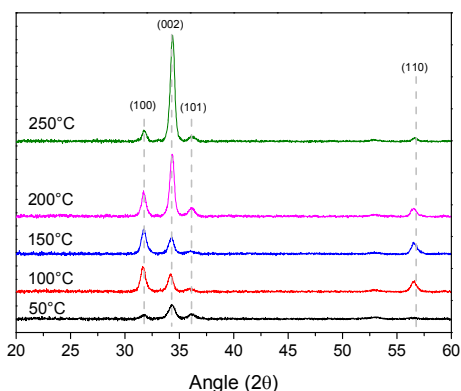


Figure 10: XRD spectra of ZnO films grown at different temperatures.

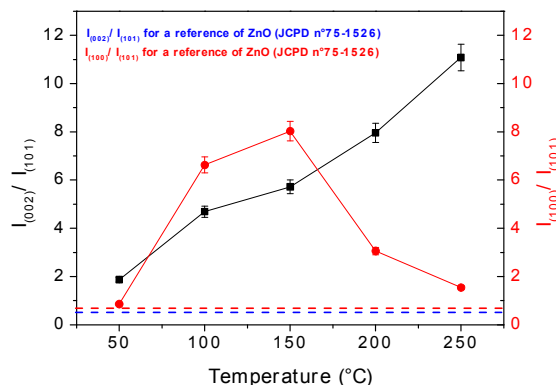


Figure 11: Ratio of the intensities of the two peaks (002)/(101) versus the growth temperature.

Table 4: Lattice parameters for the hexagonal wurtzite structure of ZnO films grown at different temperatures.

ZnO hexagonal wurtzite structure		
Deposition temperature	a=b (Å) (±0.7 Å)	c (Å) (±0.1 Å)
50 °C	3,25	5,22
100 °C	3,26	5,24
150 °C	3,25	5,23
200 °C	3,25	5,22
250 °C	3,25	5,21

This confirms further our hypothesis of growing crystalline ZnO together with a segregated amorphous ZnO_xH_y phase at very low temperature (<100°C). This latter phase inhibits the photocatalytic performance and quenches the photoluminescence of ZnO, as measured. Increasing the deposition temperature reduces substantially the fraction of the amorphous phase with a significant improvement of the photocatalytic and luminescence properties. This overall schematic picture of the crystallographic morphology of the obtained thin films is depicted in figure 12. The slow photodegradation rate for the grown ZnO at low temperatures can be attributed to the recombination of photo-generated e^-h^+ pairs at the grain-boundaries or within the H induced defects in the ZnO_xH_y amorphous phase. Both grain boundaries and the amorphous hydrogenated phase are reduced substantially for grown ZnO at elevated temperatures, which triggers the improvement of the ZnO photocatalytic activity. In addition, this study reveals a change of the ZnO texture, varying from the (100) orientation at low temperature to the (002) orientation at high temperatures. The (002) plane is a Zn terminated polar plane with high surface energy, while the (100) plane is a non polar plane with low surface energy⁵¹. Consequently, water and its contaminants will adsorb preferentially on the (002) surfaces than on the (100), which is

favourable for the degradation of water pollutants, as depicted figure 13. Water contact angle analysis highlights the wettability change as a function of the growth temperature of ZnO and the (002)/(101) crystalline orientation ratio. We can distinguish in figure 14 a clear increase of the hydrophilicity of the ZnO surfaces with their growth temperature. This variation of hydrophilicity might be directly related to the grain size evolution and the texture in the (002) orientation^{52,53}. In our case, the contribution of the grain size is not likely to be relevant since the increase of the surface roughness as a function of the growth temperature is marginal. Polar organic molecules, such as methylene blue, adsorb preferentially on polar surfaces (following a dipolar process). Therefore, the adsorption will be promoted on ZnO surfaces grown at elevated temperatures, which is favourable for their photocatalytic degradation. Bekermann *et al.* already shown that an increase of the hydrophilicity of ZnO surfaces could also improve their photodegradation performances⁵⁴.

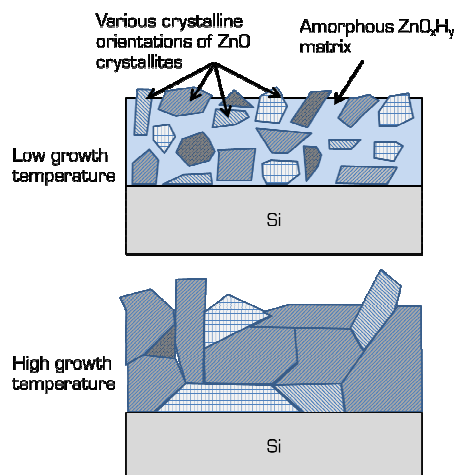


Figure 12: Schematic representation of the mechanism proposed for the growth of ZnO by ALD at low and high temperature. At low temperature, small crystallites with different orientations are embedded in an amorphous matrix of $Zn_xO_yH_z$. At high temperature, crystallites are larger and mainly oriented in the (002) plan. The amorphous phase has disappeared.

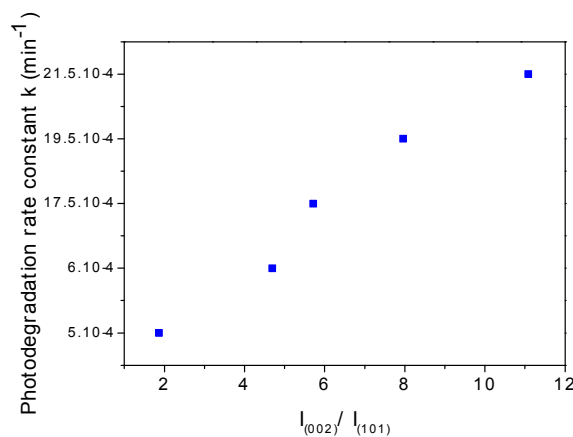


Figure 13: Photodegradation rate constant of the different ZnO films as a function of the texturation of the ZnO thin films.

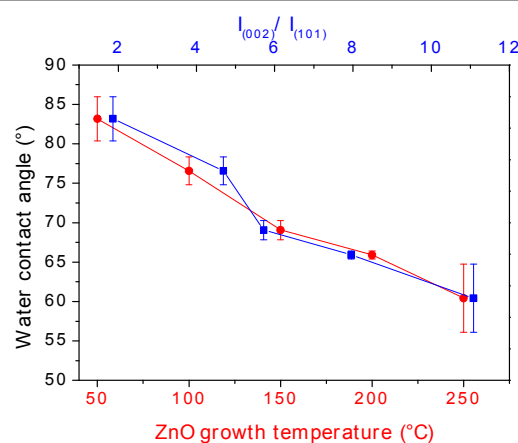


Figure 14: Water contact angle of the ZnO films grown at different temperatures.

Conclusions

We demonstrated in this work the impact of the ALD growth temperature on the properties of ZnO thin films. We showed that low temperature ZnO processes lead to ZnO polycrystalline structures and a preferred (100) orientation. The performed analyses suggest strongly the presence of an amorphous $Zn_xO_yH_z$ phase as a matrix. The highest ZnO crystallinity was obtained at high growth temperatures, where the amorphous $Zn_xO_yH_z$ phase is no more detected and a preferred (002) orientation emerges. The optical and photocatalytic properties are highly dependent to the chemical composition and the structure of the ZnO layer. In fact, the (002) texture promotes the wettability of the ZnO surface while suppressing the amorphous hydrogenated phase improves the optical properties. Both aspects enhance the photocatalytic properties of ZnO that exhibits the highest recorded degradation rate of methylene blue when grown at 250 °C.

Acknowledgment

The authors would like to thank the “Fond National de la Recherche luxembourgeoise” for the financial support of the NaneauII project (project number C10/SR/799 842) and the Visicat project (project number INTER/NSF/MAT/11/01). We also would like to thank Joffrey Didierjean for XPS analyses and his help on the interpretation of the results, as well as Stéphanie Girod for the AFM measurements.

Notes and references

^a Luxembourg Institute of Science and Technology (LIST), 5 avenue des Hauts-Fourneaux, L-4362 Esch/Alzette, Luxembourg

^b Institut de Chimie et Procédés pour l’Energie, l’Environnement et la Santé (ICPEES), UMR 7515, 25 rue Becquerel, 67087 Strasbourg cedex 2, France

^c Institut de Physique et Chimie des Matériaux de Strasbourg (IPCMS), UMR 7504, 23 rue du Loess, 67034 Strasbourg cedex 2, France

* Corresponding author e-mail:

damien.lenoble@list.lu

- D. Bahnemann, *Sol. Energy*, 2004, **77**, 445–459.
- M. Willander, O. Nur, J. R. Sadaf, M. I. Qadir, S. Zaman, A. Zainelabdin, N. Bano and I. Hussain, *Materials (Basel)*, 2010, **3**, 2643–2667.
- Y. Zhang, M. K. Ram, E. K. Stefanakos and D. Y. Goswami, *J. Nanomater.*, 2012, **2012**.
- K. D. Bhatte, D. N. Sawant, R. a. Watile and B. M. Bhanage, *Mater. Lett.*, 2012, **69**, 66–68.
- J. Hynek, V. Kalousek, R. Žouželka, P. Bezdička, P. Dzik, J. Rathouský, J. Demel and K. Lang, *Langmuir*, 2014, **30**, 380–386.
- T. J. Athauda and R. R. Ozer, *Cryst. Growth Des.*, 2013, **13**, 2680–2686.
- T. T. Ali, K. Narasimharao, I. P. Parkin, C. J. Carmalt, S. Sathasivam, S. N. Basahel, S. M. Bawaked and S. a. Al-Thabaiti, *New J. Chem.*, 2015, **39**, 321–332.
- D. Barreca, A. P. Ferrucci, A. Gasparotto, C. Maccato, C. Maragno and E. Tondello, *Chem. Vap. Depos.*, 2007, **13**, 618–625.
- D. Barreca, A. Gasparotto, C. Maccato, E. Tondello, U. L. Štangar and S. R. Patil, *Surf. Coatings Technol.*, 2009, **203**, 2041–2045.
- T. Lv, L. Pan, X. Liu and Z. Sun, *Catal. Sci. Technol.*, 2012, **2**, 2297.
- J. Becker, K. R. Raghupathi, J. St. Pierre, D. Zhao and R. T. Koodali, *J. Phys. Chem. C*, 2011, **115**, 13844–13850.
- X. Li, J. Wanga, J. Yang, J. Lang, S. Lu, M. Wei, X. Meng, C. Kou and X. Li, *J. Alloys Compd.*, 2013, **580**, 205–210.
- A. Nageswara Rao, B. Sivasankar and V. Sadasivam, *J. Hazard. Mater.*, 2009, **166**, 1357–1361.
- C. Hariharan, *Appl. Catal. A Gen.*, 2006, **304**, 55–61.
- U. Pal and P. Santiago, *J. Phys. Chem. B*, 2005, **109**, 15317–15321.
- M. Bouloudenine, N. Viart, S. Colis and a. Dinia, *Catal. Today*, 2006, **113**, 240–244.
- K. H. Tam, C. K. Cheung, Y. H. Leung, a. B. Djurišić, C. C. Ling, C. D. Beling, S. Fung, W. M. Kwok, W. K. Chan, D. L. Phillips, L. Ding and W. K. Ge, *J. Phys. Chem. B*, 2006, **110**, 20865–20871.
- N. M. Flores, U. Pal and A. Sandoval, *RSC Adv.*, 2014, **4**, 41099–41110.
- U. Ozgür, Y. I. Alivov, C. Liu, a. Teke, M. a. Reshchikov, S. Doğan, V. Avrutin, S.-J. Cho and H. Morkoç, *J. Appl. Phys.*, 2005, **98**, 041301.
- J. Liu, W. Wu, S. Bai and Y. Qin, *ACS Appl. Mater. Interfaces*, 2011, **3**, 4197–4200.
- S. Hussain, Y. Khan, V. Khranovskyy, R. Muhammad and R. Yakimova, *Prog. Nat. Sci. Mater. Int.*, 2013, **23**, 44–50.
- R. Hong, H. Qi, J. Huang, H. He, Z. Fan and J. Shao, *Thin Solid Films*, 2005, **473**, 58–62.
- K.-Y. Pan, Y.-H. Lin, P.-S. Lee, J.-M. Wu and H. C. Shih, *J. Nanomater.*, 2012, **2012**, 1–6.
- I. A. Ji, M. Park, J. Jung, M. J. Choi, Y. Lee, J. Lee and J. H. Bang, *Bull. Korean Chem. Soc.*, 2012, **33**, 2200–2206.
- E. Guziewicz, I. a. Kowalik, M. Godlewski, K. Kopalko, V. Osinniy, A. Wójcik, S. Yatsunenko, E. Łusakowska, W. Paszkowicz and M. Guziewicz, *J. Appl. Phys.*, 2008, **103**.
- Y. S. Kim, Y. S. Won, H. Hagelin-Weaver, N. Omenetto and T. Anderson, *J. Phys. Chem. A*, 2008, **112**, 4246–4253.
- N. Taewook, K. Jae-Min, K. Min-Kyu, K. Hyungjun and K. Woo-Hee, *J. Korean Phys. Soc.*, 2011, **59**, 452.
- A. Houas, H. Lachheb, M. Ksibi, E. Elaloui, C. Guillard and J. Herrmann, 2001, **31**, 145–157.
- U. G. Akpan and B. H. Hameed, *J. Hazard. Mater.*, 2009, **170**, 520–529.
- J. C. Colmenares and R. Luque, *Chem. Soc. Rev.*, 2014, **43**, 765–78.
- P. Liu, W. Li and J. Zhang, *J. Phys. Chem. C*, 2009, **113**, 14279–14284.
- Y. Cao, J. Chen, H. Zhou, L. Zhu, X. Li and Z. Cao, **024002**.
- M. J. Height, S. E. Pratsinis, O. Mekasuwandumrong and P. Praserthdam, *Appl. Catal. B Environ.*, 2006, **63**, 305–312.
- W. Shen, Z. Li, H. Wang, Y. Liu, Q. Guo and Y. Zhang, *J. Hazard. Mater.*, 2008, **152**, 172–175.
- M. Y. Guo, A. M. C. Ng, F. Liu, A. B. Djurišić, W. K. Chan, H. Su and K. S. Wong, *J. Phys. Chem. C*, 2011, **115**, 11095–11101.
- X. Zhang, J. Qin, Y. Xue, P. Yu, B. Zhang, L. Wang and R. Liu, *Sci. Rep.*, 2014, **4**, 4596.
- P. a. Rodnyi and I. V. Khodyuk, *Opt. Spectrosc.*, 2011, **111**, 776–785.
- M. Wang and L. Zhang, *Mater. Lett.*, 2009, **63**, 301–303.
- M. Balestrieri, G. Ferblantier, S. Colis, G. Schmerber, C. Ulhaq-Bouillet, D. Muller, a. Slaoui and a. Dinia, *Sol. Energy Mater. Sol. Cells*, 2013, **117**, 363–371.
- J. Petersen, C. Brimont, M. Gallart, O. Crégut, G. Schmerber, P. Gilliot, B. Hönerlage, C. Ulhaq-Bouillet, J. L. Rehspringer, C. Leuvrey, S. Colis, a. Slaoui and a. Dinia, *Microelectronics J.*, 2009, **40**, 239–241.
- M. Liu, a. H. Kitai and P. Mascher, *J. Lumin.*, 1992, **54**, 35–42.
- P. Erhart, K. Albe and A. Klein, *Phys. Rev. B*, 2006, **73**, 205203.
- X. L. Wu, G. G. Siu, C. L. Fu and H. C. Ong, *Appl. Phys. Lett.*, 2001, **78**, 2285.
- H. Zhou, H. Alves, D. M. Hofmann, W. Kriegseis, B. K. Meyer, G. Kaczmarczyk and a. Hoffmann, *Appl. Phys. Lett.*, 2002, **80**, 210–212.
- G. P. Daniel, V. B. Justinvictor, P. B. Nair, K. Joy, P. Koshy and P. V. Thomas, *Phys. B Condens. Matter*, 2010, **405**, 1782–1786.
- J. Zhang, H. Yang, Q. Zhang, H. Jiang, J. Luo, J. Zhou and S. Dong, *Appl. Phys. A*, 2014, 663–669.

Journal Name

- 47 J. Petersen, C. Brimont, M. Gallart, G. Schmerber, P. Gilliot, C. Ulhaq-Bouillet, J. L. Rehspringer, S. Colis, C. Becker, A. Slaoui and A. Dinia, *J. Appl. Phys.*, 2010, **107**, 2–7.
- 48 J. F. Moulder, J. Chastain and R. C. King, *Handbook of X-ray photoelectron spectroscopy: a reference book of standard spectra for identification and interpretation of XPS data*, Perkin-Elmer Eden Prairie, MN, 1992.
- 49 A. Janotti and C. G. Van de Walle, *Reports Prog. Phys.*, 2009, **72**, 126501.
- 50 JCPDS data sheet number 75-1526
- 51 J. H. Zeng, B. Bin Jin and Y. F. Wang, *Chem. Phys. Lett.*, 2009, **472**, 90–95.
- 52 J. Zhang, W. Huang and Y. Han, *Langmuir*, 2006, **22**, 2946–2950.
- 53 V. Khranovskyy, T. Ekblad, R. Yakimova and L. Hultman, 2012, 8146–8152.
- 54 D. Bekermann, A. Gasparotto, D. Barreca, A. Devi, R. a. Fischer, M. Kete, U. L. Štangar, O. I. Lebedev, C. Maccato, E. Tondello and G. van Tendeloo, *ChemPhysChem*, 2010, **11**, 2337–2340.